

## Graphene-Encapsulated Magnetic Nanoparticles for Safe and Steady Delivery of Ferulic Acid in Diabetic Mice

Baihua Zhong<sup>1,†,‡</sup>, Adán Mateu-Roldán<sup>2,3,‡</sup>, Mónica L. Fanarraga<sup>4,‡,\*</sup>, Wei Han<sup>5</sup>, Débora Muñoz-Guerra<sup>4</sup>, Jesús González<sup>4,6</sup>, Lu Tao Weng<sup>7</sup>, M. Ricardo Ibarra<sup>2,3,8,9</sup>, Clara Marquina<sup>2,3,\*</sup>, King Lun Yeung<sup>1,5,\*</sup>

<sup>1</sup>*Department of Chemical and Biological Engineering, The Hong Kong University of Science and Technology, Clear Water Bay, Kowloon, Hong Kong, China*

<sup>2</sup>*Instituto de Nanociencia y Materiales de Aragón (INMA), CSIC-Universidad de Zaragoza, 50009-Zaragoza, Spain.*

<sup>3</sup>*Departamento de Física de la Materia Condensada, Facultad de Ciencias, Universidad de Zaragoza, 50009-Zaragoza, Spain.*

<sup>4</sup>*Grupo de Nanomedicina, Instituto Valdecilla-IDIVAL, Universidad de Cantabria, 39011-Santander, Spain*

<sup>5</sup>*Division of Environment and Sustainability, The Hong Kong University of Science and Technology, Clear Water Bay, Kowloon, Hong Kong, China*

<sup>6</sup>*Departamento de Ciencias de la Tierra y Física de la Materia Condensada (CITIMAC), Universidad de Cantabria, 39005-Santander, Spain*

<sup>7</sup>*Material Preparation and Characterization Facility, The Hong Kong University of Science and Technology, Clear Water Bay, Kowloon, Hong Kong, China*

<sup>8</sup>*Instituto de Nanociencia de Aragón (INA), Universidad de Zaragoza, 50018-Zaragoza, Spain*

<sup>9</sup>*Laboratorio de Microscopías Avanzadas (LMA), Universidad de Zaragoza, 50018-Zaragoza, Spain*

### ORCID numbers

Fanarraga, M.L.: 0000-0003-4754-311X

González, J.: 0000-0002-0381-6393

Ibarra, M.R.: 0000-0003-0681-8260

Han, W.: 0000-0002-4808-0711

Marquina, C.: 0000-0003-0602-492X

Yeung, K.L.: 0000-0002-6970-8483

---

<sup>‡</sup> these authors contributed equally.

<sup>†</sup> new address: *Materials and Interfaces Center, Shenzhen Institutes of Advanced Technology, Chinese Academy of Sciences, Shenzhen 518055 (P. R. China).*

### \*Corresponding authors:

K.L. Yeung: Department of Chemical and Biological Engineering & Division of Environment and Sustainability, The Hong Kong University of Science and Technology, Clear Water Bay, Kowloon, Hong Kong, phone: 852 2358 7123; e-mail: kekyeung@ust.hk

M.L. Fanarraga: Grupo de Nanomedicina, Instituto Valdecilla-IDIVAL, Facultad de Medicina, Avda. Cardenal Herrera Oria, s/n, Universidad de Cantabria, 39011-Santander, Spain; phone: + 34 942 202067; e-mail: monica.lopez@unican.es

C. Marquina: Instituto de Nanociencia y Materiales de Aragón (INMA) & Departamento de Física de la Materia Condensada, Facultad de Ciencias, Universidad de Zaragoza, C/Pedro Cerbuna 12, 50009-Zaragoza, Spain; phone: +34 976 761213; e-mail: clara@unizar.es.

## ABSTRACT

New therapies demand drug delivery systems with added functionalities and proven safety, stability, and biocompatibility to achieve effective drug delivery and uptake. Herein, a magnetic nanovector (Fe@C) was designed by encapsulating iron nanoparticles within a shell of 3-10 graphene layers. The shell serves as an impervious barrier, mitigating toxicity and enhancing the biocompatibility of Fe@C. Its internalization, subcellular behavior, biocompatibility, and influence on cell viability and proliferation were investigated. Studies on human lung (adenocarcinomic human alveolar basal epithelial) and skin (epidermoid carcinoma) cells indicate Fe@C is less toxic and more biocompatible than the magnetite nanoparticles coated by an amorphous carbon (Fe<sub>3</sub>O<sub>4</sub>@C), a popular drug carrier. Fe<sub>3</sub>O<sub>4</sub>@C exhibited more signs of degradation than Fe@C when exposed to murine macrophages (mouse monocyte-macrophages J774). Unlike Fe<sub>3</sub>O<sub>4</sub>@C, Fe@C has a high drug loading capacity (0.18 g/g) for ferulic acid, an active pharmaceutical ingredient found in the traditional Chinese herb *Angelica sinensis* and releases the drug at a constant dosing rate of 8.75 mg/g/day over 30 days. Ferulic acid released by Fe@C injected subcutaneously in diabetic BALB/c mice is effective in lowering the blood glucose level.

**KEYWORDS:** drug delivery, diabetic mice, carbon-coated magnetic nanoparticles, graphene, cytotoxicity

## 1. INTRODUCTION

Nanomaterials have revolutionized life science and medicine by providing new diagnostic, therapeutic, and research tools. Nowadays, nanoparticles improve existing treatments with accurate targeting, programmed delivery, enhanced bioavailability, and reduced toxicity. It has the desired effect of improving drug efficacy while eliminating side effects [1]. Maintaining a constant dose is essential not only for the therapy's potency but also for its safety. A regular dosing rate could eliminate the need for repeated administration of medications and improve patient compliance. Therefore, a drug delivery system that can afford a constant dosing rate would be essential.

Core-shell magnetic nanoparticles promise to be an ideal vehicle for targeted drug delivery. Its large surface can host different drugs, therapeutics, and targeting agents [2], while the magnetic core can guide and localize the nanoparticles at the target site [3, 4]. It also permits imaging by MRI [4, 5] and heating by an externally applied radiofrequency magnetic field [5, 6]. The latter can remotely adjust the dosing rate at the target site or be used as a therapeutic tool to locally ablate and kill malignant cells and tissues by magnetic field hyperthermia [6].

Magnetic iron oxides are the most common core material studied [7, 8] and can be prepared with various properties through different synthesis routes. The shell must be optimized to carry the therapeutic cargo and overcome the physiological barrier to achieve the best therapeutic result [7-9]. Polymers, liposomes, and micelles are suitable drug carriers. Their high cost and poor stability are real drawbacks [2], while inorganic materials, except for silicas and carbons [10, 11], are less biocompatible. Carbons and carbonaceous materials find application in dental, orthopedic, and cardiovascular medicine, particularly in transcutaneous

implants [11, 12]. They proved sufficiently inert to host *in vitro* proliferation of multipotential mesenchymal stem cells [13, 14].

The first use of iron nanoparticles and activated carbon for drug delivery dates back to the late 1990s [15]. Hence, numerous studies on various forms of carbons have been reported [16-18]. The group's prior work [19-24] investigated carbon-coated magnetic nanoparticles prepared by a physical synthesis procedure derived from the Krätschmer-Huffman method [25]. These studies included their biocompatibility and bio-distribution in animals (i.e., murine and New Zealand rabbits) [19, 20] and plants (e.g., Cucurbitaceae) [21-23]. Their use as a drug carrier is demonstrated for doxorubicin, a potent chemotherapy drug [20, 24]. These nanoparticles concentrate in organ tissues near the implanted magnet [20].

A recent study reports that carbons' stability in various biological compartments depends on their nature and form, with surface defects playing a crucial role [26]. Therefore, the carbon shell's local structure, defects, and chemistry of the carbon-shell have vital implications on its toxicity. The magnetic iron nanoparticles (Fe@C) prepared by the Krätschmer-Huffman method are distinguished by the presence of encapsulating graphene-like layers around the magnetic iron core. Analyses using advanced microscopy and spectroscopy techniques will provide detailed information on the carbon shell's structure and chemistry. At the same time, X-ray diffraction and magnetization measurements will reveal the core properties.

Fe@C's toxicity is investigated for adenocarcinomic human alveolar basal epithelial cells, human epidermoid carcinoma cells, and murine monocyte-macrophage J774. The nanoparticle's toxicity in macrophages was studied by flow cytometry and electron microscopy. Meanwhile, the subcellular compartmentation and its influences on intracellular

chemistry were followed by transmission electron microscopy and Raman spectroscopy, respectively. Fe@C as a drug carrier was investigated for ferulic acid (FA), an active phytopharmaceutical derived from *Angelica sinensis*, a widely used herb in Chinese medicine [27, 28]. FA is a potent free radical scavenger with well-established antioxidant and anti-inflammatory properties [29, 30] that gave it antidiabetic property [30]. The high loading capacity of Fe@C for ferulic acid and linear release rates proved to be beneficial in lowering the blood glucose level in diabetic BALB/c mice.

## **2. EXPERIMENTAL METHODS**

### **2.1. Krättschmer-Huffman synthesis of carbon-coated iron nanoparticles, Fe@C**

The Fe@C nanoparticles were produced in a cylindrical arc-discharge plasma furnace [25, 31]. The fine spherical iron powder (< 10  $\mu\text{m}$ , 99.9+%, Alfa Aesar) was placed in a 30 mm hollow cylindrical graphite electrode that served as the stationary anode with a graphite rod as the moveable cathode. Both electrodes were made from graphite rods (99.9995%, Alfa Aesar), measuring 6.15 mm diameter x 102 mm length. Arc generated by the electrodes rapidly sublimed the iron and carbon into the helium atmosphere to deposit on the chamber's surface. The collected powder was purified by dissolving the uncoated iron nanoparticles in 3 M HCl. Repeated washing with excess distilled water and separation by 3 kOe permanent magnet removes the acid and spurious carbons (mainly amorphous carbon) from the remaining powder. Fe@C was obtained after drying overnight to remove the moisture.

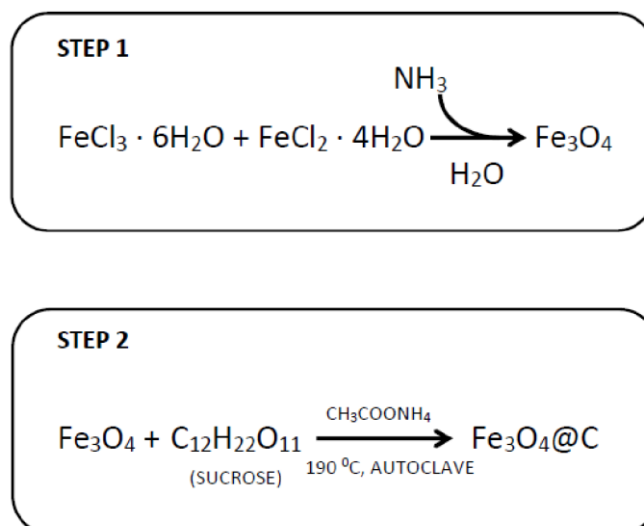


**Figure 1.** Two-step synthesis of  $\text{Fe}_3\text{O}_4@\text{C}$  involving the synthesis of the  $\text{Fe}_3\text{O}_4$  core nanoparticles (STEP 1) and the deposition of a carbon-shell (STEP 2).

## 2.2. Chemical synthesis of carbon-coated magnetite nanoparticles, $\text{Fe}_3\text{O}_4@\text{C}$

The procedure for preparing  $\text{Fe}_3\text{O}_4@\text{C}$  was adopted from Zhao et al. [32] with modifications described in Fig. 1. First, the magnetite nanoparticles were prepared by a co-precipitation method reported by De Matteis et al. [33]. Briefly, the iron salts,  $\text{FeCl}_3 \cdot 6\text{H}_2\text{O}$  (97%) and  $\text{FeCl}_2 \cdot 4\text{H}_2\text{O}$  (98%) purchased from Sigma were dissolved in water in a 3:1 ratio before adding the required amount of 30%  $\text{NH}_3 \cdot \text{H}_2\text{O}$  (Fluka) drop by drop under constant stirring. The reaction will turn the color of the solution from orange to black indicating particle formation. The suspension was sonicated for a few seconds and then left to rest for 10 min. The magnetite was recovered from the solution by a magnet and repeatedly washed to remove reaction residues. It was resuspended in 10 ml distilled water before adding a 25 ml solution containing a stoichiometric amount of sucrose (Reagent, Aldrich) and ammonium acetate (30%, Panreac). The mixture was placed in a 50-mL-Teflon-sealed autoclave and

heated at 463 K for 12 h. The product was collected from the solution with an external magnet and washed several times with distilled water to obtain the Fe<sub>3</sub>O<sub>4</sub>@C.

### 2.3. Analysis of the shell material

**Transmission Electron Microscopy (TEM)** of the samples was done under a bright-field (BT) imaging in FEI Tecnai T20 operated at 200 kV. High-Resolution TEM (HRTEM) images were obtained using an FEI Tecnai F30 operated at 300 kV, equipped with a Field Emission Gun and a SuperTwin® objective lens spatial resolution below 0.19 nm. **Raman Spectroscopy** was performed in a Confocal Raman Alpha 300 M+ from WITec, which combines a Raman spectrograph with a confocal microscope. The analysis was conducted under a 532 nm laser with a 1 μm spot size and 0.6 mW. The confocal microscope limits the incoming radiation from out-of-focus planes giving better quality signals and enables smaller lateral resolution than conventional optical microscopes.

### 2.4. Analysis of the core material

**X-Ray Diffraction (XRD)** was taken with a D-Max Rigaku instrument equipped with a rotating Cu anode (40 kV, 80 mA) and a graphite monochromator ( $K\alpha_1 = 1.5405 \text{ \AA}$ ). The diffraction was recorded between 10° and 80° at a 0,03° step and 1s per step. **Magnetic Characterization** was performed in a high sensitivity magnetometer MPMS-5S (Quantum Design Inc. USA) with a superconducting quantum interference detector (SQUID). The temperature dependence of the magnetization (5 to 350 K) was measured in a magnetic field

of 50 Oe. The magnetization isotherms were measured at 350 K in a DC magnetic field up to 5 T.

## **2.5. Fe@C and Fe<sub>3</sub>O<sub>4</sub>@C toxicity to macrophage and human cells**

Adenocarcinomic human alveolar basal epithelial cells (A549, ATCC® CCL-185™) and epidermoid carcinoma cells (A431, ATCC® CRL-1555™) modeled for inhalation and skin contact hazards. The cell lines were grown in Dulbecco's modified Eagle's medium (DMEM) supplemented with 10% fetal bovine serum (FBS, Gibco) at 310 K in a humidified atmosphere containing 5% CO<sub>2</sub>. Subculture of confluent monolayers was conducted in 0.05% trypsin (HyClone), 0.53 mM EDTA Hanks balanced salt solution (HBSS) free of calcium and magnesium. Prominent dome formation appeared two days post-confluence by phase-contrast microscopy. MTT assay determined the cell viability and carried out in triplicates for each Fe@C and Fe<sub>3</sub>O<sub>4</sub>@C loading and exposure time.

Mouse monocyte-macrophage J774 cell lines were cultured in Iscove's Modified Dulbecco's Medium (IMDM, Pan Biotech) supplemented by 10% serum with antibiotics (Gibco, Thermo Fisher Scientific) at 310 K in a humid atmosphere with 5% CO<sub>2</sub>. The cells exposed to 50 µg/mL of Fe@C or Fe<sub>3</sub>O<sub>4</sub>@C were analyzed by a Becton Dickinson FACSCanto™ II flow cytometry to measure the cell viability and life stages at different times after exposure. The untreated cells served as the negative control group. This approach allows for simultaneous multi-parametric cellular level measurements of 5,000-10,000 cells per sample. The cells were stained with propidium iodide for quantitative staining of DNA, thereby determining the cell proliferation cycle as well as fractional DNA content ("sub-G1" peak) that

indicates apoptosis [34]. Data quantification and analysis were done on FACS Diva software (Becton Dickinson, NJ, USA).

The interactions of magnetic nanoparticles and the macrophages were observed from the cells' ultrathin sections under the JEOL JEM 1011 microscope [34, 35]. For this, pellets of macrophages were fixed with 1% glutaraldehyde (Grade I, 25 % in H<sub>2</sub>O, Sigma-Aldrich) in 0.12 M phosphate buffer followed by washing in the buffer solution. Post-fixed in 1% buffered osmium tetroxide (Sigma-Aldrich), the cells were dehydrated before embedding in Araldite for ultrathin sectioning. The ultrathin sections (ca. 70 nm) of the cells were placed on copper grids and stained with lead citrate-uranyl acetate. The macrophages exposed to Fe@C and Fe<sub>3</sub>O<sub>4</sub>@C were also examined by a Raman spectrometer (T64000) Infrastructure MALTA CONSIDER, equipped with a 514 nm laser. The spectra were taken at 3 mW at 3 accumulations per measurement and each lasting 90 s.

## **2.6. Loading and release profile of ferulic acid from Fe@C and Fe<sub>3</sub>O<sub>4</sub>@C**

Ferulic acid (European Pharmacopoeia) was purchased from Sigma-Aldrich. FA was loaded by suspending 10 mg of magnetic nanoparticles in a milliliter of ethanol (absolute, Fluka) and mixing it with a 2 mg/ml FA in ethanol for Fe@C nanoparticles and 1 mg/ml FA in ethanol for Fe<sub>3</sub>O<sub>4</sub>@C nanoparticles. The mixture was shaken at room temperature and using a 3 kOe permanent magnet; the magnetic nanoparticles were drawn to the bottom of the container to analyze the supernatant by a UV-Vis spectrometer where FA has a peak of 321 nm and a shoulder at 278 nm [54]. FA was released from the loaded magnetic nanoparticles by suspending 1 mg of the samples in 1 ml of PBS solution. The suspension was kept at 310 K under gentle shaking. Similarly, the nanoparticles were separated by a magnet, and a UV-Vis

spectrometer monitored the released FA in the solution. The concentration of the adsorbed drug was calculated from the intensity of the peaks in the UV spectrum.

## **2.7. Therapeutic Properties of FA and FA/Fe@C in Diabetic Mice**

The HKUST Plant and Animal Care Facility supplied twenty-four healthy, 6-8 weeks old, male Balb/c mice weighing 23-25 g. The mice were kept under specific pathogen-free conditions, with a standard diet and water ad libitum for one week to acclimatize before the study. The mice's fasting blood glucose was measured and recorded. Eighteen mice were intraperitoneally injected with 0.2 ml of alloxan at a dose of 250 mg per Kg body weight to induce diabetes. The 10 mg.ml<sup>-1</sup> alloxan monohydrate (Sigma-Aldrich) was freshly dissolved in 0.90 wt.% salines. The remaining six mice serving as the negative control group were injected with 0.2 ml physiological saline. Hyperglycemia, a symptom of diabetic Mellitus developed within a week of induction, was confirmed by daily blood glucose monitoring. Mice with a fasting blood glucose level above 16.7 mM were considered a successful diabetic model for hyperglycemia [36]. Among the eighteen diabetic mice, six mice served as the positive control group, and the remaining twelve mice were treated with FA and FA/Fe@C. A 5 mg.ml<sup>-1</sup> FA freshly dissolved in saline was injected into six diabetic mice with a daily dose of 50 mg.Kg<sup>-1</sup> (1 mg per 20 g) for a week (FA-treatment group). FA/Fe@C was injected subcutaneously into the remaining six diabetic mice (FA/Fe@C-treatment group) at the same FA dose of 50 mg.Kg<sup>-1</sup>. The mice were carefully sterilized after administration, and the mice's blood glucose level was monitored daily.

### 3. RESULTS AND DISCUSSION

#### 3.1. Fe@C and Fe<sub>3</sub>O<sub>4</sub>@C nanoparticles

Figure 2A presents the detailed structure of Fe@C nanoparticles obtained by Krätschmer-Huffman synthesis in an arc-discharge plasma furnace from ultrahigh purity carbons and high purity iron. The high-resolution TEM image displays the Fe core with a dark contrast, and the C shell being a lighter element, appears in a lighter shade. It shows the shell cladding the magnetic iron nanoparticle to be continuous layers of graphene. The graphene shell is formed during the energetic events of the synthesis when the temperature in the arc discharge can exceed 3273 K. The graphene layers deposit on iron's passivated interface as it condenses in the furnace's inert helium atmosphere. The iron core is ferromagnetic, as shown by its magnetization isotherm at room temperature (cf. *Fig. S1* in Supplementary Information, SI). According to the XRD data (cf. *Fig. S2* in SI), the core's primary phase is  $\alpha$ -Fe.

In contrast, the Fe<sub>3</sub>O<sub>4</sub>@C prepared by the two-steps process has an amorphous carbon shell surrounding the core particle, as shown in Fig. 2B. The core is superparamagnetic at room temperature and is Fe<sub>3</sub>O<sub>4</sub> magnetite (cf. *Figs. S3* and *S4* in SI). The Fe@C nanoparticle core is quasi-spherical, while the magnetite in Fe<sub>3</sub>O<sub>4</sub>@C has a polyhedral shape. More images of Fe@C and Fe<sub>3</sub>O<sub>4</sub>@C are presented in *Figs. S5* and *S6* of SI. Analysis of the TEM images by ImageJ software [37] and OriginPro 2015 graphics program shows Fe@C display a Lorentzian size distribution and a mean particle size of 21 nm (cf. *Fig. S7* in SI). Particles larger than 30 nm are present, but none are larger than 80 nm. Fe<sub>3</sub>O<sub>4</sub>@C sizes also fit a Lorentzian distribution curve with an average size of 14 nm (cf. *Fig. S8* in SI).

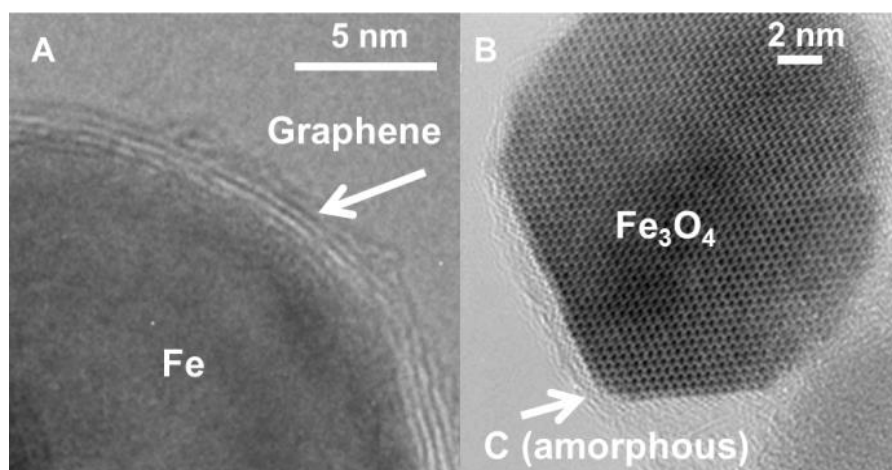


**Figure 2.** High-resolution transmission electron micrographs of (A) Fe@C and (B) Fe<sub>3</sub>O<sub>4</sub>@C. The arrow in (A) refer to the 5-6 graphene layers surrounding the Fe core, while the arrow in (B) points to the amorphous carbon encapsulating the Fe<sub>3</sub>O<sub>4</sub> core; the constituent atoms and atomic planes are clearly seen, showing a high degree of order.

### 3.2. Fe@C and Fe<sub>3</sub>O<sub>4</sub>@C cytotoxicity

Figure 3 reports the cytotoxicity of Fe@C and Fe<sub>3</sub>O<sub>4</sub>@C for A549 human alveolar and A431 human epidermal cells. The encapsulating shell of the magnetic nanoparticles serves as a barrier preventing the exposure of the core material that could increase toxicity to the cell. Nevertheless, the A549 displays a typical dose-response relationship to Fe@C (Fig. 3a) and Fe<sub>3</sub>O<sub>4</sub>@C (Fig. 3b), as shown by the lower cell viability for higher nanoparticle loadings and longer exposure times. Fe<sub>3</sub>O<sub>4</sub>@C has a more significant effect on cell viability. The trend is similar, but the difference is less pronounced in A431 human epidermal cells, as shown in Figs. 3c and 3d. The observed toxicity is most likely related to the generation of reactive oxygen species (ROS) that alter the chemistry of intracellular plasma activating transcription factors and cytokines. The ROS also interfere with cellular signalling pathways, affect gene transcription, and damage DNA, all of which would lower cell viability and affect the normal cell cycle.

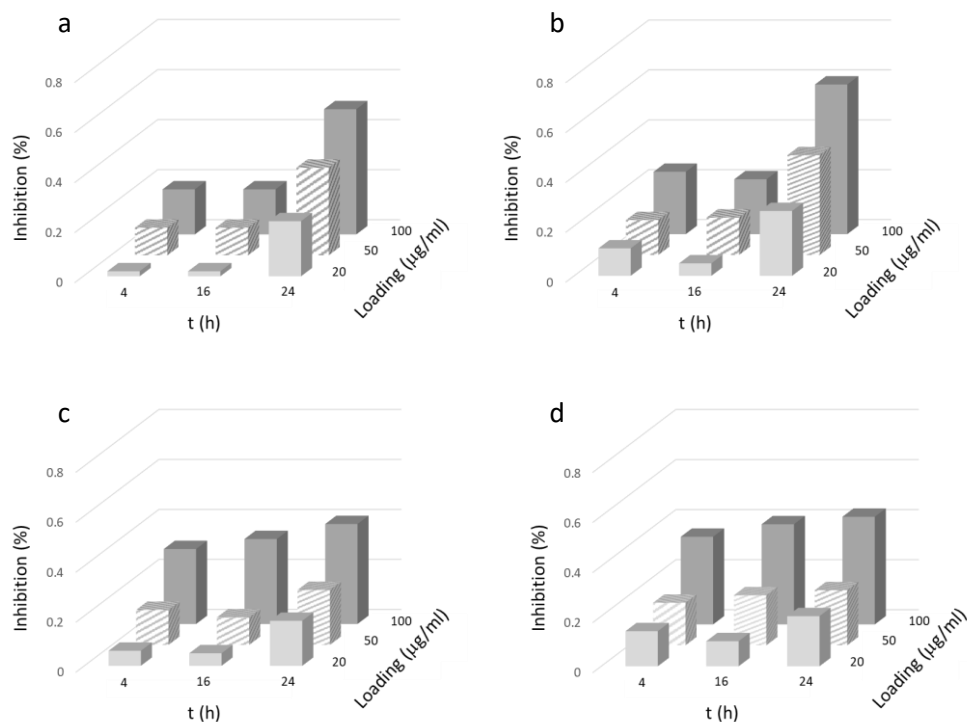


**Figure 3.** Inhibition of A549 cells exposed to (a) Fe@C and (b) Fe<sub>3</sub>O<sub>4</sub>@C, and A431 cells exposed to (c) Fe@C and (d) Fe<sub>3</sub>O<sub>4</sub>@C at 20, 50, and 100 µg/ml and 4, 16, and 24 h.

Macrophage protects by detecting foreign bodies such as nanoparticles and taking them up by endocytosis or phagocytosis. This study exposed mouse macrophage J774 cells to a reasonably high concentration of Fe@C or Fe<sub>3</sub>O<sub>4</sub>@C (50 µg/mL) for 96 h. Untreated cells were used as the negative control. The cell viability and cell cycle were assessed by flow cytometry every 24 h. Quantitative measurement of the total amount of DNA per cell determines the percentage of apoptotic cells and cells at different stages of the proliferation cycle. Figure 4 A and B show a normal cell cycle that consists of four detectable phases: (i) the “sub-G0” phase corresponding to apoptotic or necrotic cells (i.e., fragmented cells); (ii) the “G1” phase when cells that have just divided or are not undergoing cell division; (iii) the “S” phase when dividing cells are undergoing DNA synthesis; and finally, (iv) cells at “G2” phase when cell

division (mitosis) is underway, which is typically characterized by a double genome. Upon separation of the two daughter cells, the cell cycle re-starts at G1.

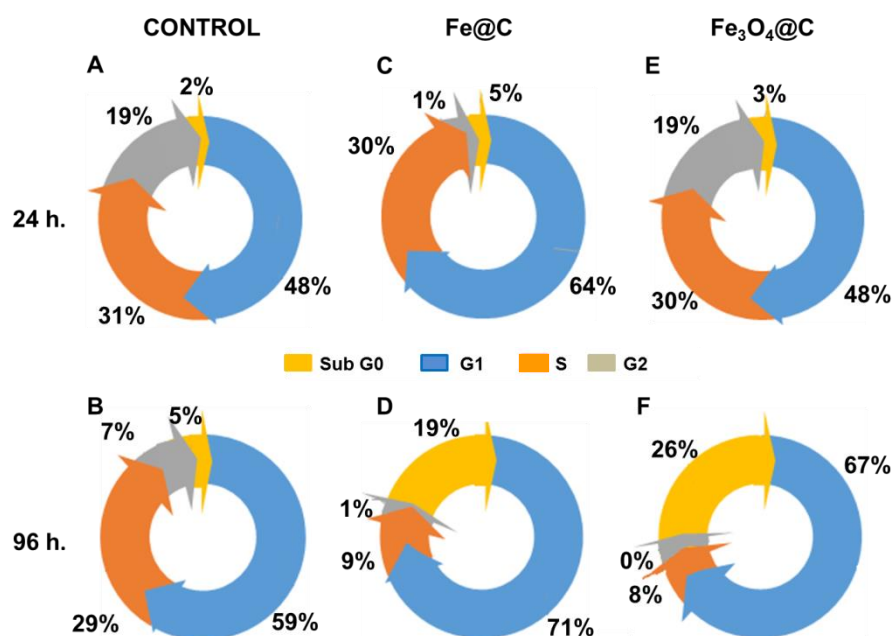


**Figure 4.** Cell population at different stages of macrophage cell cycle for (A)&(B) untreated cells serving as control; (C)&(D) cells exposed to Fe@C; (E)& (F) cells exposed to Fe<sub>3</sub>O<sub>4</sub>@C for 24 h (top row) and 96 h (bottom row).

Macrophage cells exposed to Fe@C for 24 h (Fig. 4C) and 96 h (Fig. 4D) differ from each other and the untreated control samples in the cell population (cf. Fig. S9 of SI for the original flow cytometry logarithmic plots). Exposure to Fe@C induces a putative blockage of the “G1-S” stage of the cell cycle during the first 24 h resulting in a rise in cell death after 96 h, as indicated by the higher proportion of cells at the sub-G0 phase. A partial arrest of the cell cycle in the G1-S phase is attributed to the mechanical effects from Fe@C trapped within the intracellular compartment. The change in the “S” phase of the cell cycle also suggests a partial blockage of DNA synthesis, which has also been observed for other carbon nanomaterials [38]. Figure 4E shows that macrophage cells exposed to Fe<sub>3</sub>O<sub>4</sub>@C for 24 h have similar cell

population profile as untreated cells (cf. *Fig. S10* of SI for the original flow cytometry logarithmic plots). However, an apparent decrease in S phase and an increase in apoptotic cell population after 96 h of exposure (*Fig. 4F*) indicating a significant interference with cell proliferation at this dosage.

### **3.3. Fe@C and Fe<sub>3</sub>O<sub>4</sub>@C interactions with macrophage cells**

The intracellular destination of the Fe@C and Fe<sub>3</sub>O<sub>4</sub>@C in macrophage cells following 24 h and 168 h (i.e., 7 days) is investigated to elucidate the effects on the macrophages. Under optical microscope, the treated and untreated cells have similar appearance without evident damage from the nanomaterial exposure. However, transmission electron microscope reveals Fe@C are present in the intracellular region of the macrophage cell (*Fig. 5A*) and appear as black aggregates visible in *Fig. 5B*. Fe@C are embedded within membranous structures corresponding to phagosomes or endosomal-lysosomal vesicles and in the cytosolic milieu. Although rare, the spurious presence of carbon nanotube (indicated by the arrow in *Fig. 5B* and *Fig. S11* in SI) in Fe@C could trigger their escape into the cytosol by damaging the membranes of the endosomes (or phagosomes) [35]. No detectable differences were observed in TEM images following 7 days exposure.

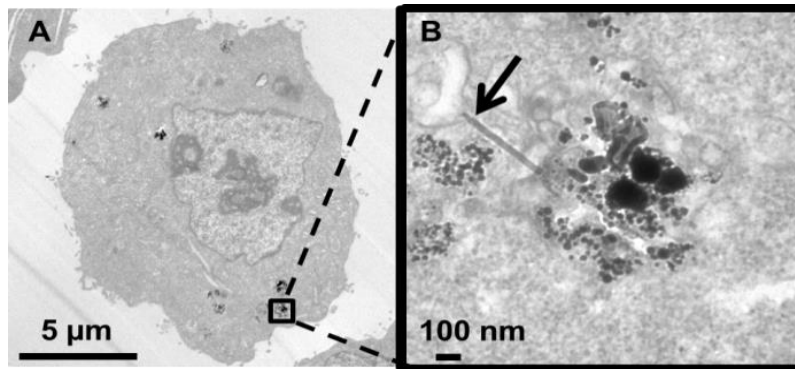


**Figure 5.** Transmission electron micrographs of (A) Fe@C inside a macrophage's cytosol after 24 h exposure, and (B) a high magnification image of a selected area in (A) showing Fe@C and a spurious carbon nanotube.

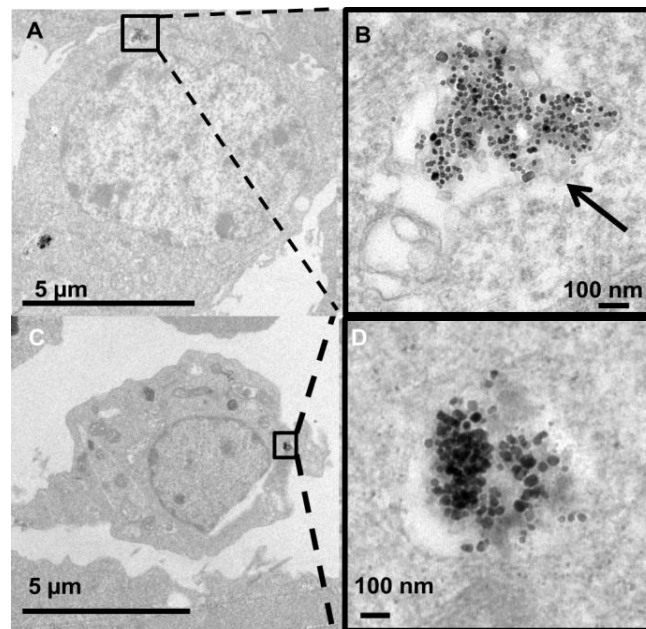


**Figure 6.** Transmission electron micrographs of macrophages exposed to Fe<sub>3</sub>O<sub>4</sub>@C for (A)&(B) 24 h and (C)&(D) 7 days. (A) Fe<sub>3</sub>O<sub>4</sub>@C nanoparticles internalized in a macrophage and (B) a higher magnification image showing Fe<sub>3</sub>O<sub>4</sub>@C at the endosome-phagosome membrane. (C) Fe<sub>3</sub>O<sub>4</sub>@C nanoparticles internalized in a macrophage 7 days after incubation and (D) Magnified region of (C) showing aggregation within intracellular membrane.

Macrophages exposed to Fe<sub>3</sub>O<sub>4</sub>@C are shown in Fig. 6. The Fe<sub>3</sub>O<sub>4</sub>@C are located inside the endosome-phagosome membranes of a healthy-looking macrophage after 24 h (Fig. 6A) and as in the case of Fe@C, the intracellular milieu does not appear to affect Fe<sub>3</sub>O<sub>4</sub>@C.

Indeed, the amorphous carbon surrounding the nanoparticles are clearly visible in the micrograph. Figure 6C displays the image of a macrophage after 7 days exposure to Fe<sub>3</sub>O<sub>4</sub>@C and the carbon matrix is less defined and appears more diffused as shown in Fig. 6D. The image is highly suggestive of a putative degradation of the amorphous carbon as macrophages are very efficient in breaking down and degrading wide range of materials captured by the endocytic or phagocytic entry routes. Their lysosomes, apart from displaying a pH of 4.5, contain a variety of enzymes (acid-hydrolases and peroxidases) that can gradually digest the carbon shell [39]. The degradation of the carbon shell in Fe<sub>3</sub>O<sub>4</sub>@C (as suggested by the TEM micrograph in Fig. 6D) could expose the Fe<sub>3</sub>O<sub>4</sub> core to dissolution increasing its toxicity to the cells (cf. Figs. 3c-d and 4e-f).

Raman spectroscopy is a powerful tool in investigating intracellular degradation of carbonaceous materials such as carbon nanotubes [39]. Figure 7A displays the Raman spectrum of Fe@C, showing peaks of pristine graphene, and those associated with defects [40, 41]. The position, shape, and relative intensity of the G and 2D peaks depend on the number of graphene layers, defects, and dopants [40, 42, 43]. The ratio of intensities  $I(2D)/I(G)$  is approximately 0.3 less than 4.0 expected from a single graphene layer [44]. It is consistent with the strained structure of the graphene layers enveloping the Fe core shown in Fig. 1A. Furthermore, the Raman spectrum is like the one observed by Serrano-Esparza et al. [45] for graphene deposited on metals. It suggests that the metallic iron core has a strong influence on the deposited graphene shell.

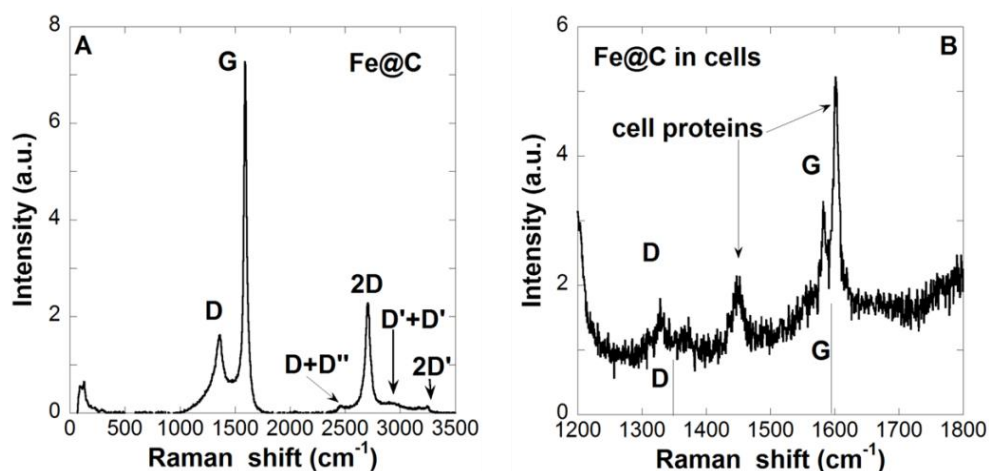


**Figure 7.** Raman spectra of (A) as-synthesized Fe@C and (B) internalized Fe@C in macrophage (72 h exposure). Note: letters correspond to the signals of pristine (G, D+D'' and 2D'); defective (D, 2D and D+D') graphene and the lines in (B) mark the D and G peaks location of pristine Fe@C.

The Raman signals in Fig. 7A show displaced G, D and 2D peaks of around 5 and 10  $\text{cm}^{-1}$  as a result of the strained structure of the graphene as it envelopes the high curvature surface of the magnetic iron core (ca. 21 nm). Defects are apparent from the presence of D and D + D' peaks. It is well known that the bcc structure of  $\alpha$ -Fe does not have Raman-active modes. Only in those cases in which the periodicity of the bcc crystal lattice is interrupted that the overtones of acoustic phonons ( $2\text{TA}_1$  and  $2\text{TA}_2$ ) at the edge of Brillouin zone can be observed in the Raman spectrum [46]. The absence of such signals in the figure confirms the bcc structure of the Fe cores and their excellent crystallinity.

Figure 7B presents the Raman spectrum taken of the macrophages exposed to 50  $\mu\text{g}/\text{mL}$  of nanoparticles for 72 h. TEM study indicates that macrophage cells contain sufficient loading of Fe@C for Raman analysis. The spectrum displays the characteristic G and D peaks from the graphene shell and weak signals belonging to cell proteins at 1450  $\text{cm}^{-1}$  and the 1600  $\text{cm}^{-1}$  [34]. A detailed analysis of the cell contribution to the Raman signals is presented in Figs. S11-S14 in SI. The internalized Fe@C shows a 25  $\text{cm}^{-1}$  shift towards infrared in its D and G bands.

This is reminiscent of carbon nanotubes after oxidative treatment [39]. It is very likely that the shift is related to a charge transfer [47] resulting from the oxidation and degradation of the internalized Fe@C in the macrophage cell, albeit, the process is slow as it is not evident from the microscopy study.

Fe<sub>3</sub>O<sub>4</sub>@C has a very different carbon shell as seen in Fig. 8A with the D (near 1400 cm<sup>-1</sup>) and G (close to 1600 cm<sup>-1</sup>) bands are nearly the same intensities and heavily overlapping, which together with absence of the 2D band are signature of amorphous carbon [48]. This is confirmed by TEM observation and XRD analysis. The peak at 700 cm<sup>-1</sup> corresponds to the A<sub>1g</sub> band of magnetite, which is the most intense of the five Raman modes associated with its spinel structure [49]. The Raman spectrum of Fe<sub>3</sub>O<sub>4</sub>@C in the macrophage (Fig. 8B) displays heavily overlapped D and G bands (cf. *Figs. S15-S16 in SI*). The broadening of D and G peaks indicates there are more defects in the carbon shell of Fe<sub>3</sub>O<sub>4</sub>@C internalized by the macrophage cells. Moreover, the 20 cm<sup>-1</sup> shift towards the infrared could be related to the charge transfer accompanying the cellular processes during the degradation of the carbon shell. This is consistent with the observations made by González-Lavado et al. [39] on *in-vitro* experiments on macrophages. The cell proteins contributions at 1400 cm<sup>-1</sup> and 1600 cm<sup>-1</sup> [34] are convoluted within the two broad peaks in Fig. 8B.

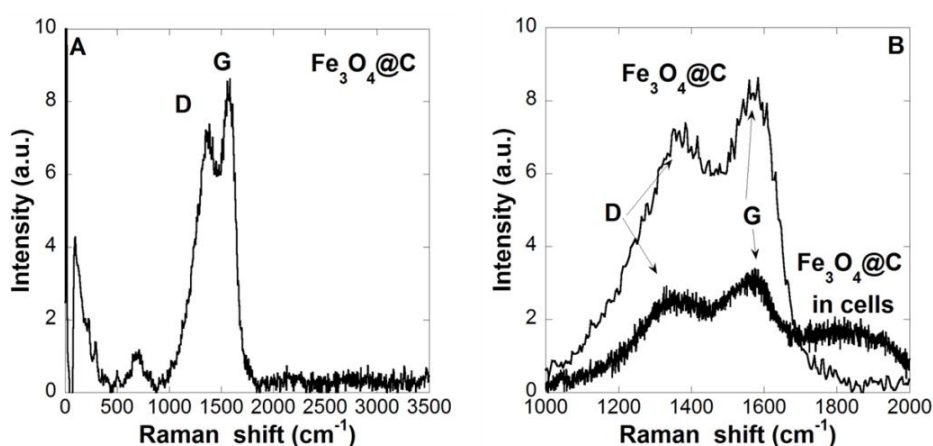


Figure 8. Raman spectra of (A) as-synthesized Fe<sub>3</sub>O<sub>4</sub>@C and (B) internalized Fe@C in macrophage (72 h exposure).

### 3.4. Fe@C and Fe<sub>3</sub>O<sub>4</sub>@C carriers for ferulic acid (FA)

The ferulic acid found in *Angelica sinensis*, an important Chinese herbal medicine [27, 28], is a potent free radical scavenger with antioxidant, anti-inflammatory, and anti-allergenic properties [29, 30]. FA is also reported to be antidiabetic and offers protection against diabetic nephropathy [50]. FA is loaded by adsorption from FA solution as shown in Fig. 9a for Fe@C and Fig. 9c for Fe<sub>3</sub>O<sub>4</sub>@C. Adsorption reaches steady state after 120 min for Fe@C with a 0.18 g/g FA loading and 2 min for Fe<sub>3</sub>O<sub>4</sub>@C with a loading of 0.07 g/g FA. Fe@C has higher adsorption capacity for FA and releases nearly all adsorbed FA (ca. 97 %) at a constant rate of 8.75 mg/g/day over 20 day as shown in Fig. 9b. A steady dosing is essential for many therapeutic applications to ensure efficacy and safety. The desorption of FA from Fe<sub>3</sub>O<sub>4</sub>@C follows a very different trend with approximately 0.6 mg of FA (slightly over 80%) released on the first day and the remaining FA desorbed over the next 29 days at 0.2 mg/g/day (ca. 94% on day 30). The rapid release could be a disadvantage in many applications, but the nonlinear release profile could find uses in hormonal therapy and even in cancer treatments.

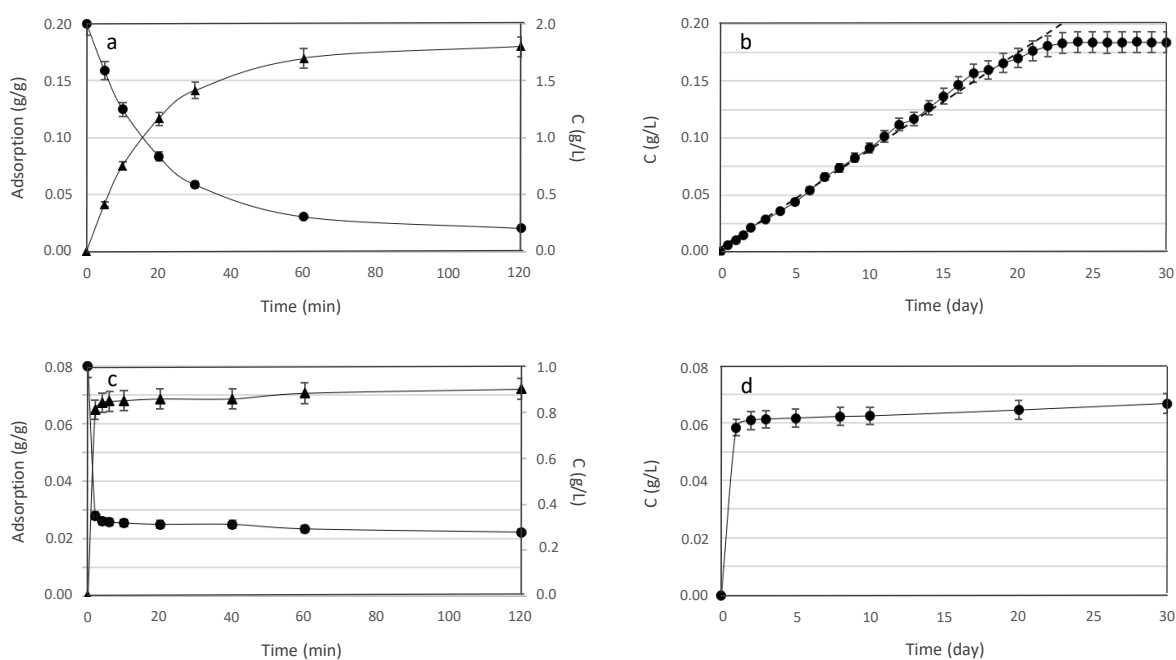


Figure 9: Adsorption or loading profile of FA on (a) Fe@C and (c) Fe<sub>3</sub>O<sub>4</sub>@C and its release from (b) Fe@C and (d) Fe<sub>3</sub>O<sub>4</sub>@C. Note: the adsorption were conducted at nanoparticle concentration of 10 mg/ml and desorption at 1 mg/ml; the circles represent FA in supernatant (right Y axis) and triangles represent the calculated amount of FA adsorbed (left Y axis) in (a) and (c).

The ToF-SIMS depth profiles in Fig. 10 shows FA adsorption on Fe@C and Fe<sub>3</sub>O<sub>4</sub>@C. The characteristic ToF-SIMS ion fragments from FA, FA/Fe@C, FA/Fe<sub>3</sub>O<sub>4</sub>@C, and FA/Fe<sub>3</sub>O<sub>4</sub> are reported in Fig. S17 of SI. The FA-OH<sup>+</sup> (m/z 177), FA<sup>+</sup> (m/z 195), and FA-H<sup>+</sup> (m/z 194) are the most abundant ion fragments from FA and are present on both FA/Fe@C and FA/Fe<sub>3</sub>O<sub>4</sub>@C. FA does not adsorb on Fe<sub>3</sub>O<sub>4</sub> and its fragments are not detected by ToF-SIMS (Fig. SXX in SI). It is important to note that Fe@C has a strong C<sup>+</sup> signal (Fig. S17 of SI) and displays intense C<sub>x</sub><sup>-</sup> signals in the negative ToF-SIMS spectrum (not shown) that is consistent with the graphitic structure of the graphene shell and in agreement with the Raman data (Fig. 7). Figure 10 plots the characteristic FA fragment, FA-OH<sup>+</sup>, with depth. FA being a hydroxycinnamic acid has a strong affinity for graphene and adsorbs in greater amount (ca. roughly twice) and depth (ca.

8 nm) on Fe@C compared to Fe<sub>3</sub>O<sub>4</sub>@C. FA is mostly adsorbed on a shallow layer (ca. 3 nm) on Fe<sub>3</sub>O<sub>4</sub>@C explaining its moderate adsorption capacity and rapid release (Figs. 9c-d).

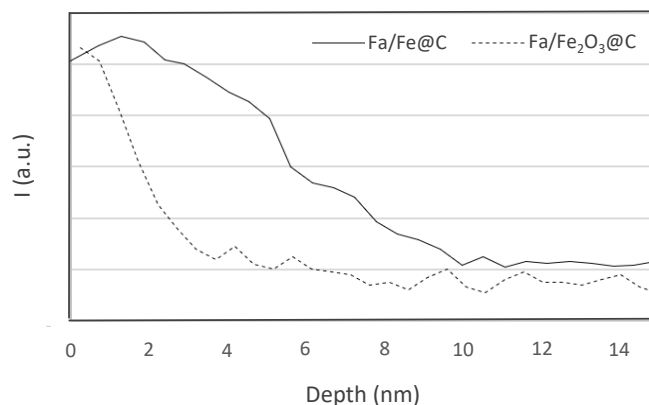


Figure 10: Plots of FA characteristic ToF-SIMS ion fragment (FA-OH)<sup>+</sup> (m/z 177) with depth by C<sub>60</sub><sup>+</sup> ion bombardment of FA adsorbed on Fe@C (solid line) and Fe<sub>3</sub>O<sub>4</sub>@C (dashed line).

### 3.5. FA and FA/Fe@C treatments of diabetic mice

Figure 11 shows healthy Balb/c mice (negative control group) have a mean blood glucose of 7.5 mM and the diabetic mice (positive control) have 24.0 mM five days after intraperitoneal injection of alloxan. On the 11<sup>th</sup> day after diabetic induction, six diabetic mice (Fa-treatment group) were injected with 5 mg/ml FA at a dose of 50 mg/Kg for seven consecutive days from day 11 to 16. This should give a C<sub>max</sub> of 500 mg/L Fa in the bloodstream. It is clear from the figure that FA decreases and finally stabilizes the blood glucose level of diabetic mice to 15.2 mM (cf. day 20 to 25) lower than the positive control group (ca. 24.0 mM). Prabhakar et al. [51] reports a comparable 40% decrease in blood glucose level in streptozotocin-treated diabetic rats treated with FA at a daily dose of 40 mg/Kg per os over 21 days. Ferulic acid's antidiabetic property arises from its ability to mitigate lipid peroxidation, lower NF-kB immunoreactivity in various organs, and enhance cell stress response as observed in alloxan-induced diabetic mice and streptozotocin-induced diabetic

rats [52, 53]. Furthermore, FA increases plasma insulin, hepatic glycogen synthesis, and glucokinase activity resulting in lower blood glucose in diabetic mice [54-55]. FA being an efficient free radical scavenger protects against organ damages caused by overproduction of ROS from hyperglycemia [56].

Onishi et al. [57] observed that streptozotocin-induced diabetic ICR mice fed daily with 0.01 % FA mixed in their powdered basal diets (ca. 0.3-0.6 mg FA or 3-6 mg/Kg) over a period of six weeks have 20 % lower blood glucose than the control group on normal diets. Oral administration of FA may not be efficient according to a study on Sprague-Dawley rats (180-220 g) [58] fed on *Angelica sinensis*' radix (6.48 mg/Kg FA). The FA reaches  $C_{max}$  of  $0.44 \pm 0.11$  mg/L and distributes rapidly to various organs ( $t_{1/2\alpha} = 3.90 \pm 0.78$  min). It cleared from the bloodstream with an elimination half-life ( $t_{1/2\beta}$ ) of  $45.78 \pm 6.22$  min. A constant dosing of FA into the bloodstream could be more effective. Thus, six mice (Fa/Fe@C-treatment group) were injected subcutaneously with 6 mg FA/Fe@C giving an equivalent dose of 50 mg FA/Kg on day 11. It is estimated from the release profile of FA/Fe@C in Fig. 9b that 0.053 mg FA was released daily into the bloodstream (ca. 26.2 mg/L) from the FA/Fe@C embedded under the skin. Although this is only 5% of FA administered to mice in the FA-treatment group and less than a fifth of the amount of FA in Onishi's study [57], this amount is sufficient to gradually decrease the blood glucose from 23.2 mM to below 19.6 mM as shown in Fig. 11. This moderate decrease of 16% is comparable to observations made by Ohnishi et al. [57].

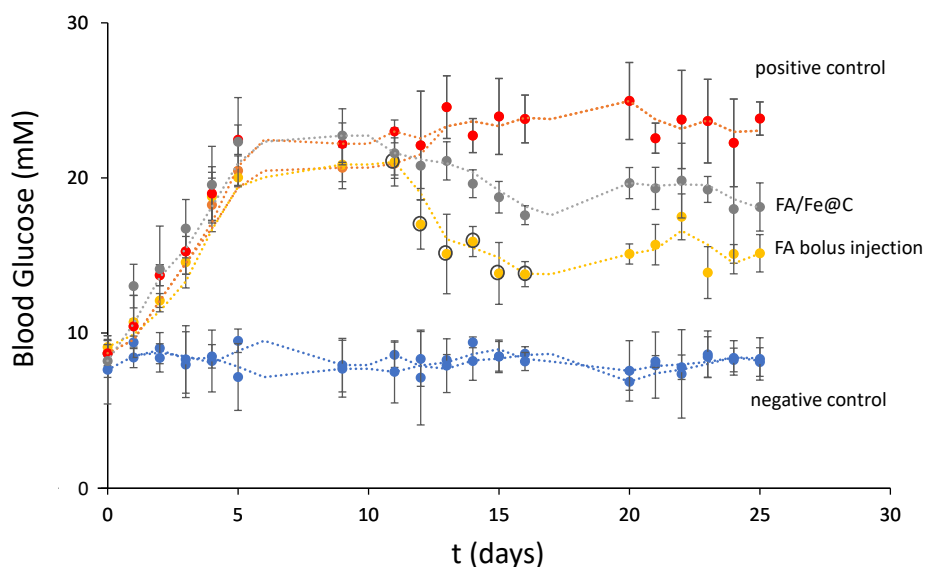


Figure 11: Plots of blood glucose of healthy Balb/c mice (negative control group), alloxan-induced diabetic mice (positive control group), FA-treated diabetic mice (FA-treatment group) and Fa/Fe@C-treated diabetic mice (FA/Fe@C-treatment group). Note: six mice in each group and triplicate blood measurements.

## CONCLUSIONS

A detailed study of Fe@C with graphene shell and magnetic iron core prepared by arc-discharge method has been presented and compared to the more traditional Fe<sub>3</sub>O<sub>4</sub>@C with amorphous carbon shell and magnetite core prepared by two-steps solvothermal process. To assess their suitability as magnetic nano-carriers for drugs, their interactions with macrophage cells have been studied. TEM images show that the macrophage cells successfully engulfed the Fe@C and Fe<sub>3</sub>O<sub>4</sub>@C, localizing the nanoparticles inside endolysosomes-phagosomes. However, the presence of spurious carbon nanotubes in Fe@C trigger their escape into the cytosol. There are no evident signs of cellular damage even after 7 days exposure to Fe@C and Fe<sub>3</sub>O<sub>4</sub>@C despite a putative “S” cell-cycle phase blockage observed from 96 h exposure to the nanomaterials.

Raman spectra of the cell cultures following 72 h exposure to the nanoparticles revealed the appearance of defects in the carbon shell indicating degradation by the macrophage and hence its biocompatibility. The process is however slow, and the cores remained protective even after 7 days in macrophage cells. This is important as metallic iron can cause ROS that can lead to cell death through oxidative damage of biomolecules [79], and magnetite (as well as maghemite) catalyzes the decomposition of  $H_2O_2$  to produce hydroxyl radicals through peroxidase-like activity under the acidic conditions inside the lysosomes [80]. Study on human lung and skin cell lines show Fe@C has low cytotoxicity consistent with the macrophage study. In a separate study, New Zealand rabbits intravenously injected with Fe@C survived 18 months bio-distribution study [38]. The results confirmed the biocompatibility of Fe@C during their progressive elimination (presumably, through urine and faeces) throughout the experiment. It confirms that the graphene layers coating protects the Fe cores for months, despite the appearance of the defects in the macrophage cell study.

The study shows that both graphene and amorphous carbon shells are suitable carrier for ferulic acid. Fe@C can carry twice the FA cargo compared to  $Fe_3O_4@C$  and release its cargo in a linear manner at a constant rate of 8.75 mg/g/day.  $Fe_3O_4@C$  displays a more typical nonlinear release profile and delivers most of the FA within a day.

## **AKNOWLEDGEMENTS**

This work is supported by the Horizon 2020 BIORIMA project and the Hong Kong Research Grant Council E-HKUST601/17 and Dr. B.H. Zhong is a recipient of the HKJEBN Scholarship and his stay at INA is supported by the HKUST Overseas Research Award. The team is also grateful

for the funding from the Spanish Ministerio de Economía y Competitividad (MINECO) through projects MAT2013-42551, PI16/00496, PI19/00349, and DTS19/00033, co-funded by ERDF/ESF, "Investing in Your Future". The authors also thank the CSIC (through the project PIE 201960E119 and the Regional Government of Aragón (DGA) for financial support through grant E28\_20R. The authors acknowledge the support and the use of the installations of the Advanced Microscopy Laboratory (LMA) and the Servicio General de Apoyo a la Investigación of the University of Zaragoza along with the Material Characterization and Preparation Facility (MCPF), the Environmental Central Facility (ENVF), and the Animal and Plant Care Facility (APCF) at the Hong Kong University of Science and Technology.

## REFERENCES

- [1] M. Arruebo, M. Galan, N. Navascues, C. Tellez, C. Marquina, M.R. Ibarra, J. Santamaria, Development of magnetic nanostructured silica-based materials as potential vectors for drug-delivery applications, *Chemistry of Materials* 18(7) (2006) 1911-1919.
- [2] M. Arruebo, R. Fernandez-Pacheco, M.R. Ibarra, J. Santamaria, Magnetic nanoparticles for drug delivery, *Nano Today* 2(3) (2007) 22-32.
- [3] B.B. Yellen, Z.G. Forbes, D.S. Halverson, G. Fridman, K.A. Barbee, M. Chorny, R. Levy, G. Friedman, Targeted drug delivery to magnetic implants for therapeutic applications, *Journal of Magnetism and Magnetic Materials* 293(1) (2005) 647-654.
- [4] I. Urries, C. Munoz, L. Gomez, C. Marquina, V. Sebastian, M. Arruebo, J. Santamaria, Magneto-plasmonic nanoparticles as theranostic platforms for magnetic resonance imaging, drug delivery and NIR hyperthermia applications, *Nanoscale* 6(15) (2014) 9230-9240.
- [5] J.W.M. Bulte, D.L. Kraitchman, Iron oxide MR contrast agents for molecular and cellular imaging, *NMR in Biomedicine* 17(7) (2004) 484-499.
- [6] T.E. Torres, E. Lima, M.P. Calatayud, B. Sanz, A. Ibarra, R. Fernandez-Pacheco, A. Mayoral, C. Marquina, M.R. Ibarra, G.F. Goya, The relevance of Brownian relaxation as power absorption mechanism in Magnetic Hyperthermia, *Scientific Reports* 9 (2019) 11.
- [7] A.S. Lubbe, C. Bergemann, W. Huhnt, T. Fricke, H. Riess, J.W. Brock, D. Huhn, Preclinical experiences with magnetic drug targeting: Tolerance and efficacy, *Cancer Research* 56(20) (1996) 4694-4701.
- [8] S. Goodwin, C. Peterson, C. Hoh, C. Bittner, Targeting and retention of magnetic targeted carriers (MTCs) enhancing intra-arterial chemotherapy, *Journal of Magnetism and Magnetic Materials* 194(1-3) (1999) 132-139.
- [9] M. Gidwani, A.V. Singh, Nanoparticle Enabled Drug Delivery Across the Blood Brain Barrier: in vivo and in vitro Models, Opportunities and Challenges, *Current Pharmaceutical Biotechnology* 14(14) (2013) 1201-1212.
- [10] T. Yu, A. Malugin, H. Ghandehari, Impact of Silica Nanoparticle Design on Cellular Toxicity and Hemolytic Activity, *Acs Nano* 5(7) (2011) 5717-5728.
- [11] A. Carranza-Bencano, J.R. Armas-Padron, M. Gili-Miner, M.A. Lozano, Carbon fiber implants in osteochondral defects of the rabbit patella, *Biomaterials* 21(21) (2000) 2171-2176.
- [12] R. De Santis, D. Prisco, A. Apicella, L. Ambrosio, S. Rengo, L. Nicolais, Carbon fiber post adhesion to resin luting cement in the restoration of endodontically treated teeth, *Journal of Materials Science-Materials in Medicine* 11(4) (2000) 201-206.
- [13] M. Blazewicz, Carbon materials in the treatment of soft and hard tissue injuries, *European Cells and Materials* (2) (2001) 21-9.
- [14] J. Lopez Penalver, J.-L. Linares-Fernandez, V. de Araujo Farias, M. Victoria Lopez-Ramon, M. Tassi, F. Javier Oliver, C. Moreno-Castilla, J. Mariano Ruiz de Almodovar, Activated carbon cloth as support for mesenchymal stem cell growth and differentiation to osteocytes, *Carbon* 47(15) (2009) 3574-3577.
- [15] C.A. Bittner, S.C. Goodwin, C.K. Hoh, J.W. Sayre, Feasibility of magnetically directing a novel iron and activated carbon drug-carrier microparticle as a potential method to enhance intra-arterial chemotherapy, *Radiology* 205 (1997) 1025-1025.
- [16] A.A. Kuznetsov, V.I. Filippov, O.A. Kuznetsov, V.G. Gerlivanov, E.K. Dobrinsky, S.I. Malashin, New ferro-carbon adsorbents for magnetically guided transport of anti-cancer drugs, *Journal of Magnetism and Magnetic Materials* 194(1-3) (1999) 22-30.
- [17] X.-W. Hua, Y.-W. Bao, F.-G. Wu, Fluorescent Carbon Quantum Dots with Intrinsic Nucleolus-Targeting Capability for Nucleolus Imaging and Enhanced Cytosolic and Nuclear Drug Delivery, *ACS applied materials & interfaces* 10(13) (2018) 10664-10677.
- [18] D. Wang, Y. Ren, Y. Shao, D. Yu, L. Meng, Facile Preparation of Doxorubicin-Loaded and Folic Acid-Conjugated Carbon Nanotubes@Poly(N-vinyl pyrrole) for Targeted Synergistic Chemo Photothermal Cancer Treatment, *Bioconjugate Chemistry* 28(11) (2017) 2815-2822.

- [19] E. Escribano, R. Fernandez-Pacheco, J. Gabriel Valdivia, M. Ricardo Ibarra, C. Marquina, J. Queralt, Effect of Magnet Implant on Iron Biodistribution of Fe@C Nanoparticles in the Mouse, *Archives of Pharmacal Research* 35(1) (2012) 93-100.
- [20] C. Marquina, M.R. Ibarra, Carbon Encapsulated Functional Magnetic Nanoparticles for Life Sciences, in: P.K. Zarzycki (Ed.), *Pure and Functionalized Carbon Based Nanomaterials*, CRC Press 2020.
- [21] P. Gonzalez-Melendi, R. Fernandez-Pacheco, M.J. Coronado, E. Corredor, P.S. Testillano, M.C. Risueno, C. Marquina, M.R. Ibarra, D. Rubiales, A. Perez-De-Luque, Nanoparticles as smart treatment-delivery systems in plants: Assessment of different techniques of microscopy for their visualization in plant tissues, *Annals of Botany* 101(1) (2008) 187-195.
- [22] E. Corredor, P.S. Testillano, M.-J. Coronado, P. Gonzalez-Melendi, R. Fernandez-Pacheco, C. Marquina, M. Ricardo Ibarra, J.M. de la Fuente, D. Rubiales, A. Perez-de-Luque, M.-C. Risueno, Nanoparticle penetration and transport in living pumpkin plants: in situ subcellular identification, *Bmc Plant Biology* 9 (2009).
- [23] Z. Cifuentes, L. Custardoy, J.M. de la Fuente, C. Marquina, M. Ricardo Ibarra, D. Rubiales, A. Perez-de-Luque, Absorption and translocation to the aerial part of magnetic carbon-coated nanoparticles through the root of different crop plants, *Journal of Nanobiotechnology* 8 (2010).
- [24] R. Fernandez-Pacheco, C. Marquina, J. Gabriel Valdivia, M. Gutierrez, M. Soledad Romero, R. Cornudella, A. Laborda, A. Vilorio, T. Higuera, A. Garcia, J. Antonio Garcia de Jalon, M. Ricardo Ibarra, Magnetic nanoparticles for local drug delivery using magnetic implants, *Journal of Magnetism and Magnetic Materials* 311(1) (2007) 318-322.
- [25] W. Kratschmer, L.D. Lamb, K. Fostiropoulos, D.R. Huffman, SOLID C-60 - A NEW FORM OF CARBON, *Nature* 347(6291) (1990) 354-358.
- [26] E. Gonzalez-Lavado, N. Iturrioz-Rodriguez, E. Padin-Gonzalez, J. Gonzalez, L. Garcia-Hevia, J. Heuts, C. Pesquera, F. Gonzalez, J.C. Villegas, R. Valiente, M.L. Fanarraga, Biodegradable multi-walled carbon nanotubes trigger anti-tumoral effects, *Nanoscale* 10(23) (2018) 11013-11020.
- [27] S.Y. Ou, K.C. Kwok, Ferulic acid: pharmaceutical functions, preparation and applications in foods, *Journal of the Science of Food and Agriculture* 84(11) (2004) 1261-1269.
- [28] B.H. Wang, J.P. Ou-Yang, Pharmacological actions of sodium ferulate in cardiovascular system, *Cardiovascular Drug Reviews* 23(2) (2005) 161-172.
- [29] M. Srinivasan, A.R. Sudheer, V.P. Menon, Ferulic acid: Therapeutic potential through its antioxidant property, *Journal of Clinical Biochemistry and Nutrition* 40(2) (2007) 92-100.
- [30] M. Ramar, B. Manikandan, T. Raman, A. Priyadarsini, S. Palanisamy, M. Velayudam, A. Munusamy, N.M. Prabhu, B. Vaseeharan, Protective effect of ferulic acid and resveratrol against alloxan-induced diabetes in mice, *European Journal of Pharmacology* 690(1-3) (2012) 226-235.
- [31] H.R. Rechenberg, J.A.H. Coaquira, C. Marquina, B. Garcia-Landa, M.R. Ibarra, A.M. Benito, W. Maser, E. Munoz, M.T. Martinez, Mossbauer and magnetic characterisation of carbon-coated small iron particles, *Journal of Magnetism and Magnetic Materials* 226 (2001) 1930-1932.
- [32] H. Zhao, H.-J. Cui, M.-L. Fu, A general and facile method for improving carbon coat on magnetic nanoparticles with a thickness control, *Journal of Colloid and Interface Science* 461 (2016) 20-24.
- [33] L. De Matteis, L. Custardoy, R. Fernandez-Pacheco, C. Magen, J.M. de la Fuente, C. Marquina, M. Ricardo Ibarra, Ultrathin MgO Coating of Superparamagnetic Magnetite Nanoparticles by Combined Coprecipitation and Sol-Gel Synthesis, *Chemistry of Materials* 24(3) (2012) 451-456.
- [34] J.C. Villegas, L. Alvarez-Montes, L. Rodriguez-Fernandez, J. Gonzalez, R. Valiente, M.L. Fanarraga, Multiwalled Carbon Nanotubes Hinder Microglia Function Interfering with Cell Migration and Phagocytosis, *Advanced Healthcare Materials* 3(3) (2014) 424-432.
- [35] N. Iturrioz-Rodriguez, E. Gonzalez-Dominguez, E. Gonzalez-Lavado, L. Marin-Caba, B. Vaz, M. Perez-Lorenzo, M.A. Correa-Duarte, M.L. Fanarraga, A Biomimetic Escape Strategy for Cytoplasm Invasion by Synthetic Particles, *Angewandte Chemie-International Edition* 56(44) (2017) 13736-13740.
- [36] Z. Zhang, J. Jiang, P. Yu, X. Zeng, J. Larrick, Y. Wang, Hypoglycemic and Beta Cell Protective Effects of Andrographolide Analogue for Diabetes Treatment, *Journal of Translational Medicine* 7(1) (2009) 62-70.

- [37] C.A. Schneider, W.S. Rasband, K.W. Eliceiri, NIH Image to ImageJ: 25 years of image analysis, *Nature Methods* 9(7) (2012) 671-675.
- [38] L. Garcia-Hevia, R. Valiente, J. Gonzalez, J.L. Fernandez-Luna, J.C. Villegas, M.L. Fanarraga, Anti-Cancer Cytotoxic Effects of Multiwalled Carbon Nanotubes, *Current Pharmaceutical Design* 21(15) (2015) 1920-1929.
- [39] E. Gonzalez-Lavado, N. Iturrioz-Rodriguez, E. Padin-Gonzalez, J. Gonzalez, L. Garcia-Hevia, J. Heuts, C. Pesquera, F. Gonzalez, J.C. Villegas, R. Valiente, M.L. Fanarraga, Biodegradable multi-walled carbon nanotubes trigger anti-tumoral effects, *Nanoscale* 10(23) (2018) 11013-11020.
- [40] A.C. Ferrari, Raman spectroscopy of graphene and graphite: Disorder, electron-phonon coupling, doping and nonadiabatic effects, *Solid State Communications* 143(1-2) (2007) 47-57.
- [41] A.C. Ferrari, D.M. Basko, Raman spectroscopy as a versatile tool for studying the properties of graphene, *Nature Nanotechnology* 8(4) (2013) 235-246.
- [42] S. Pisana, M. Lazzeri, C. Casiraghi, K.S. Novoselov, A.K. Geim, A.C. Ferrari, F. Mauri, Breakdown of the adiabatic Born-Oppenheimer approximation in graphene, *Nature Materials* 6(3) (2007) 198-201.
- [43] J. Yan, Y.B. Zhang, P. Kim, A. Pinczuk, Electric field effect tuning of electron-phonon coupling in graphene, *Physical Review Letters* 98(16) (2007) 4.
- [44] A.C. Ferrari, J.C. Meyer, V. Scardaci, C. Casiraghi, M. Lazzeri, F. Mauri, S. Piscanec, D. Jiang, K.S. Novoselov, S. Roth, A.K. Geim, Raman spectrum of graphene and graphene layers, *Physical Review Letters* 97(18) (2006) 4.
- [45] I. Serrano-Esparza, J. Fan, J.M. Michalik, L. Alfredo Rodriguez, M. Ricardo Ibarra, J. Maria de Teresa, The nature of graphene-metal bonding probed by Raman spectroscopy: the special case of cobalt, *Journal of Physics D-Applied Physics* 49(10) (2016).
- [46] J. Jorge, E. Flahaut, F. Gonzalez-Jimenez, G. Gonzalez, J. Gonzalez, E. Belandria, J.M. Broto, B. Raquet, Preparation and characterization of alpha-Fe nanowires located inside double wall carbon nanotubes, *Chemical Physics Letters* 457(4-6) (2008) 347-351.
- [47] S. Gupta, M. Hughes, A.H. Windle, J. Robertson, Charge transfer in carbon nanotube actuators investigated using in situ Raman spectroscopy, *Journal of Applied Physics* 95(4) (2004) 2038-2048.
- [48] A.C. Ferrari, Raman spectroscopy of graphene and graphite: Disorder, electron-phonon coupling, doping and nonadiabatic effects, *Solid State Communications* 143(1-2) (2007) 47-57.
- [49] O.N. Shebanova, P. Lazor, Raman spectroscopic study of magnetite (FeFe<sub>2</sub>O<sub>4</sub>): a new assignment for the vibrational spectrum, *Journal of Solid State Chemistry* 174(2) (2003) 424-430.
- [50] S. Chowdhury, S. Ghosh, A.K. Das, P.C. Sil, Ferulic Acid Protects Hyperglycemia-Induced Kidney Damage by Regulating Oxidative Insult, Inflammation and Autophagy, *Frontiers in Pharmacology* 10(27) (2019) 1-24.
- [51] P.K. Prabhakar, R. Prasad, S. Ali, M. Doble, Synergistic interaction of ferulic acid with commercial hypoglycemic drug in streptozotocin induced diabetic rats, *Phytomedicine*, 20 (2013) 488-494. doi: 10.1016/j.phymed.2012.12.004.
- [52] M. Ramar, B. Manikandan, T. Raman, A. Priyadarsini, S. Palanisamy, M. Velayudam, A. Munusamy, N. Marimuthu, B. Vaseeharan, Protective effect of ferulic acid and resveratrol against alloxan-induced diabetes in mice, *European Journal of Pharmacology* 690 (2012) 226-235.
- [53] S. Roy, S.K. Metya, S. Sannigrahi, N. Rahaman, F. Ahmed, Treatment with ferulic acid to rats with streptozotocin-induced diabetes: effects of oxidative stress, pro-inflammatory cytokines, and apoptosis in the pancreatic  $\beta$  cell. *Endocrine* 44 (2013) 369-379.
- [54] E.H. Jung, S.R. Kim, I.K. Hwang, T.Y. Ha, Hypoglycemic effects of a phenolic acid fraction of rice bran and ferulic acid in C57BL/Ksj-db/db mice, *J. Agricultural Food Chemistry* 55 (2007) 9800-9804.
- [55] S. Adisakwattana, P. Chantarasinlapin, H. Thammarat, S. Anun-Yibchok, A series of cinnamic acid derivatives and their inhibitory activity on intestinal alpha-glucosidase, *Journal Enzyme Inhibition Medical Chemistry* 24 (2009) 1194-1200.
- [56] D. Badawy, H.M. El-Bassossy, A. Fahmy, A. Azhar, Aldose reductase inhibitors zopolrestat and ferulic acid alleviate hypertension associated with diabetes: effect on vascular reactivity. *Canadian Journal of Physiology and Pharmacology* 91 (2013) 101-107.

[57] M. Ohnishi, T. Matuo, T. Tsuno, A. Hosoda, E. Nomura, H. Taniguchi, H. Sasaki, H. Morishita, Antioxidant activity and hypoglycemic effect of ferulic acid in STZ-induced diabetic mice and KK-A<sup>y</sup> mice, *Biofactors* 21 (2004) 315-319.

[58] N. Yang, Z. Tang, Y.Q. Xu, X. Li, Q. Wang, Pharmacokinetic study of ferulic acid following transdermal or intragastric administration in rats, *AAPS PgarmSciTech* 21 (2020) 169.